Injection of Atoms and Molecules in a Superfluid Helium Fountain: Cu and Cu_2He_n ($n = 1, ..., \infty$)

Esa Vehmanen,[†,‡,§] Vahan Ghazarian,[‡,‖] Courtney Sams,[§] Isahak Khachatryan,[‡] Jussi Eloranta,[§] and V. A. Apkarian*,[‡]

[†]Department of Chemistry, Nanoscience Center, University of Jyväskylä, P.O. Box 35, FIN 40014, Finland

[‡]Department of Chemistry, University of California, Irvine, California 92697, United States

[§]Department of Chemistry and Biochemistry, California State University at Northridge, 18111 Nordhoff Street, Northridge, California 91330, United States

[‖]Department of Chemistry, East Los Angeles College, Monterey Park, California 91754, United States

ABSTRACT: We introduce an experimental platform designed around a thermomechanical helium fountain, which is aimed at investigating spectroscopy and dynamics of atoms and molecules in the superfluid and at its vapor interface. Laser ablation of copper, efficient cooling and transport of Cu and Cu_2 through helium vapor (1.5 K < T < 20 K), formation of linear and T-shaped Cu_2—He complexes, and their continuous evolution into large Cu_2—He_n clusters and droplets are among the processes that are illustrated. Reflection is the dominant quantum scattering channel of translationally cold copper atoms (T = 1.7 K) at the fountain interface. Cu_2 dimers mainly travel through the fountain unimpeded. However, the conditions of fountain flow and transport of molecules can be controlled to demonstrate injection and, in particular, injection into a nondivergent columnar fountain with a plug velocity of about 1 m/s. The experimental observables are interpreted with the aid of bosonic density functional theory calculations and ab initio interaction potentials.
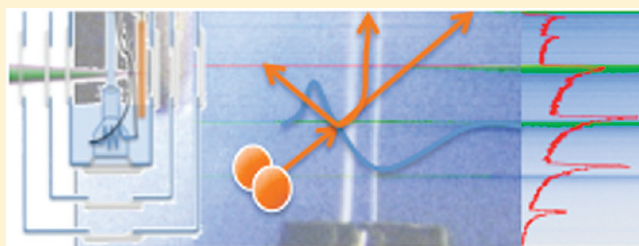
INTRODUCTION

Spectroscopic studies of molecules in superfluid helium is an advanced subject.[1,2] While driven by diverse motivations, the investigations inevitably probe implications of superfluidity on molecular scales.[3] Of the methods used, the cluster pick-up scheme has proven to be most effective.[4] And although a tremendous amount has been learned, the method has several limitations. The supersonic expansion fixes the thermodynamic $\{P,T\}$ state of clusters and eliminates temperature as a variable: a parameter that plays a key role in controlling the properties of He-II.[5,6] Moreover, at the characteristic temperature of clusters (0.37 K),[7] rotons are not thermally excited and the phonon cutoff wavelength (ca. 5 nm) implies that they can only exist in clusters with more than 10^3 atoms. This leaves the droplet surface and surface capillary waves (ripplons) as the principal source and sink of excitations, along with excitation that may be imparted during the pick-up process. It would be desirable to eliminate these constraints. To this end, we have considered several different approaches to inject molecules in bulk-like liquid. Of these, injection of laser-ablated molecules in large liquid droplets produced by pulsed supersonic expansion[8] has enabled extensions of the cluster pick-up approach.[9−12] Historically, the first spectroscopic observations of molecules in He-II were realized in the bulk liquid.[13,14] There have been significant efforts to introduce both neutrals[15−17] and ions[18] in static liquid and solid helium, including the recent spectroscopic study of copper dimers in liquid and solid helium.[19] The mundane consideration that all

molecular species freeze and phase separate at the relevant temperatures dictates transient conditions for measurements in the bulk, and methods such as laser ablation in the bulk commonly result in ill-defined thermodynamic states. A flowing liquid with a continuously refreshed volume could, in principle, overcome this limitation. It is in this context that we consider the injection of molecules in a thermomechanical superfluid fountain,[5,6,20] which is the subject of the present report.

We describe our experimental effort to inject laser ablated copper atoms and dimers in a helium fountain. Under the experimental conditions we employ, translational energies thermalized to ~1.5 K and with velocities relative to the moving surface of ~1 m/s, the injection of atoms and molecules into a flowing superfluid column raises fundamental questions regarding scattering dynamics at the ideal liquid—gas interface. For weakly interacting systems, such as Cu—He, quantum evaporation and condensation can be expected to control the interfacial scattering dynamics.[21−23] Entrainment of molecules in the flow requires momentum transfer, for which there is not an obvious mechanism in the volume of the fountain, below the critical velocity of He-II (~20 m/s). Barring vorticity, in the
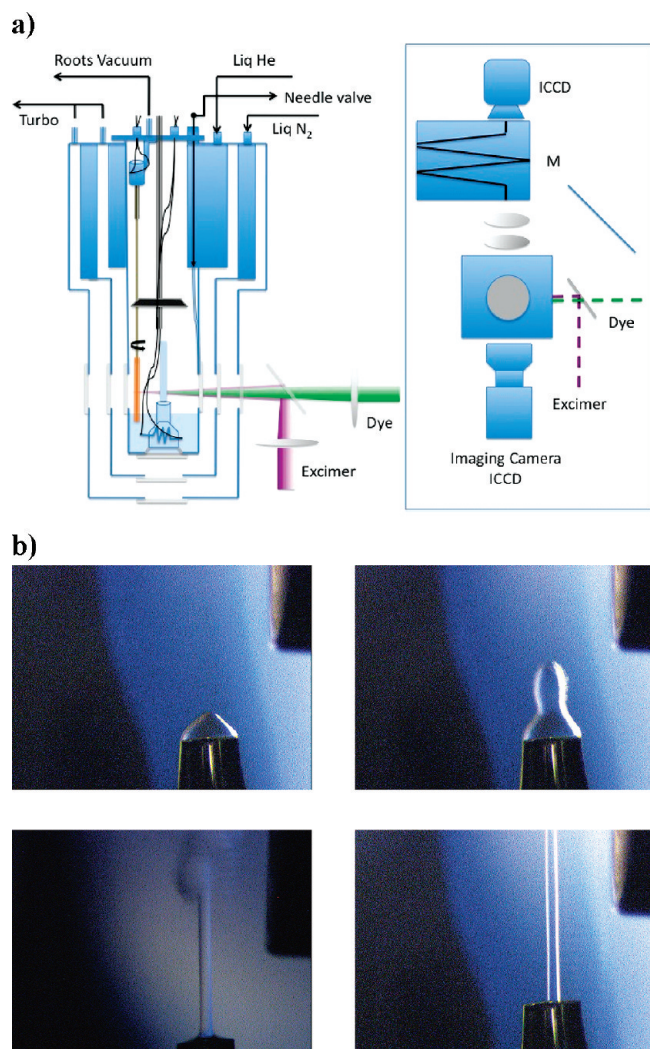
Figure 1. (a) Schematic overview of the experimental setup. A triple-walled liquid helium cryostat with optical access (windows shown in gray) is used. The fountain flow is controlled through resistive heating, the ablation target is a copper rod partially submerged in the liquid, and rotated through the vertically mounted motor. The excimer laser is used for ablation, and the dye laser is used for LIF measurements. The block diagram shows the optical arrangement. An intensified CCD array, combined with a macro lens allows imaging with time resolution of 2 ns (minimum gate width of ICCD). When employed behind the monochromator (M), the ICCD provides time-gated, spectrally resolved emission spectra. The timing between excimer, dye-laser, and detection gate is adjustable. (b) Distinct modes of operation of the thermo-mechanical fountain (small blob, large blob, misty mode, and nondivergent column flow). The fountain diameter is 200 μm.

absence of viscous drag on the translational motion of molecules, it is not clear whether they can be carried by the flow or whether they would pass through a superfluid fountain unimpeded. Once again, one can expect excitations at the liquid—gas interface to play a major role in the scattering processes, now at the gas—fountain interface at the relatively high temperature of ~1.5 K. Key to the successful implementation of these experiments is characterization of the transport and cooling of plasma ablated atoms and molecules in the cold vapor of liquid helium. Laser ablation of copper, which has been extensively investigated in different contexts,[24−26] proves particularly valuable for visualizing the relevant transport dynamics.

The characterized visible spectrum of Cu_2[27−33] makes it a convenient probe of the essential dynamical processes. Rapid cooling and neutralization of the plasma, dimer formation through three-body collisions and on droplets, rotational cooling and freeze-out of the vibrational population, subsequent pick-up of helium atoms and cluster growth are among the processes that can be tracked as a function of time and distance the molecules travel through cold helium. We outline these processes, with the main aim of reporting proof of principle: the injection of atomic Cu and molecular Cu_2 in the fountain, and the unique aspects our experimental platform offers for spectroscopic and dynamical investigations. The latter are highlighted by the accessible wealth of spectroscopic information regarding Cu_2 and Cu_2-He_n ($n = 1, ..., \infty$) clusters, which we present along with their theoretical analysis.

■ METHODS

Experimental Section. The experimental setup is shown in Figure 1a. We use a triple-walled liquid helium Dewar with an inner diameter of 7.5 cm and with optical access provided through five sets of triple windows (modified Oxford Variox). The liquid level is controlled with a needle valve, the temperature inside the cryostat is measured with a rhodium iron sensor (Oxford model T1−103), and the pressure is monitored with a capacitance manometer (MKS Baratron). The cryostat is pumped with a high speed, 300 cfm, roots vacuum pump (Alcatel Adixen), which under typical operation conditions allows the reduction of the pumped helium temperature to 1.5 K. The pumping speed is regulated with a feedback controlled throttle valve (MKS model 252) to maintain the vapor at constant pressure. The vacuum shroud is maintained at 10^{-6} Torr using a separate turbo molecular pump (Pfeiffer model TPH 062; 56 L/s of N_2). The fountain consists of a glass tube packed with 0.5−2 μm rouge (ferric oxide particles) and a 30 Ω resistive heater. The tube is drawn into a capillary with an inner diameter of 200 μm, to serve as the fountain spout. The flow rate of the fountain is controlled with the heater, relying on the thermo-mechanical effect to generate a differential pressure $\Delta P = \Delta S(T)\Delta T$, with entropy density carried by the normal fraction across the temperature gradient. The flow velocity at the spout is deduced by the height (h) of the fountain, assuming deceleration strictly due to the force of gravity: $v = (2gh)^{1/2}$. The fountain can be operated in several flow modes (see Figure 1b). A nondivergent column flow is obtained, with heights exceeding ~1 cm, at flow velocities above ~0.5 m/s. By reducing the pressure to only overcome surface tension, stationary free-standing liquid profiles ("blobs") can be generated, with residual surface flow ensuring a refreshed interface. Intermediate between these limits is the misty-top operation, the characteristics of which are determined by the speed at which the vapor is pumped. In all but the last case, a sharp liquid—gas interface is obtained, as evidenced by the light diffraction that generates the contrast in the images of Figure 1b.

Two different arrangements have been used to rotate the laser ablation target, to maintain a fresh ablation surface. In the initial studies, the target consisted of an oxygen-free high conductivity (OFHC) copper disk mounted on a motor with a horizontal shaft. The disk-to-fountain distance is adjusted, with typical operating conditions corresponding to a separation of 1−2 mm. Fluorescence imaging of the ablation products (i.e., Cu atoms and Cu_2) is used for visualizing gas dynamics post ablation. Analysis of the flow indicates convective drift due to a thermal gradient between the motor-mounted disk and the fountain. Replacement of the target with a rod suspended from a vertically mounted motor at the top of the cryostat, with the rod partially
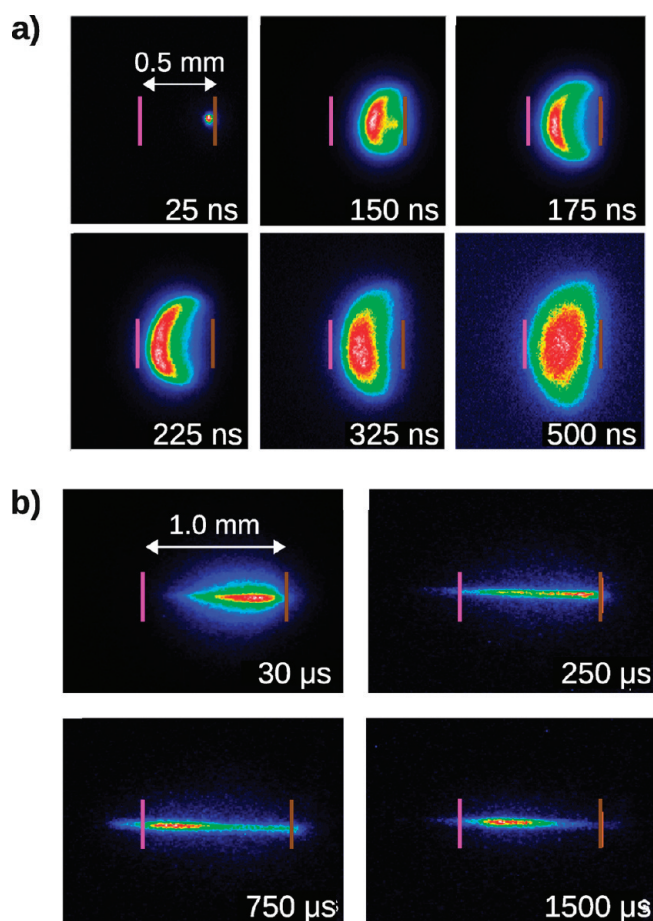
Figure 2. Spatial evolution of the ablation plume in cold helium gas (2 K temperature and 10 Torr pressure) as a function of the delay between the excimer and the doubled dye lasers (emission intensity is given in arbitrary units by contour colors with red and blue indicating high and low intensity, respectively). (a) Time-gated fluorescence images recorded by monitoring emission over the $Cu(3\,^2P^0_{3/2} \rightarrow 3\,^2D_{5/2})$ transition at 510.55 nm. The location of the copper target is indicated by a brown vertical line and the fountain was turned off (magenta line shown only for reference). b) Fluorescence images obtained by re-excitation of Cu atoms over the $4\,^2S_{1/2} \rightarrow 3\,^2P_{3/2}$ transition at 324.75 nm while monitoring the same emission as in (a). The location of the Cu target and the fountain in (b) are indicated by brown and magenta vertical lines, respectively.

submerged in the liquid reservoir (see Figure 1a), effectively eliminated the convective gas flow.

A XeCl excimer laser, operating at 308 nm and a repetition rate of 20 Hz, is used to ablate the copper (Lambda Physik EMG 101 MSC; 80 mJ/pulse). A time-delayed Nd:YAG pumped dye laser is used for the spectroscopic measurements (Continuum Surelite, Lambda Physik FL3002). The spectral width of the free running dye laser is 0.2 cm^{-1}. The line narrows down to 0.04 cm^{-1} with the insertion of an intracavity etalon. An optogalvanic cell (Sirah) is used for absolute wavelength calibration. The ablation and dye laser beams are focused with separate quartz lenses and combined using a 50/50 beam splitter. An intensified charge coupled device (ICCD; Princeton PI-MAX; 2 ns minimum gate width) camera equipped with a macro lens is used to obtain time-gated spatial images of the fluorescence. Alternatively, the laser-induced fluorescence is collected with two plano-convex lenses, dispersed in a 1/4 m

monochromator, and detected using an ICCD array to record time-gated emission spectra. Timing between the two lasers and the ICCD gate is provided by software controlled delay generators (SRS model DG 535). The system was controlled by a computer, using the libmeas package.[34]

Theory. We compute the copper dimer (within Abelian point group D_{2h}; core orbitals 1s, 2s, 2p, 3s, 3p on both atoms) ground and several low lying excited states (e.g., X, A, B, C states) around the equilibrium geometry using the closed-shell equation-of-motion (EOM) coupled clusters (CC) method with single and double excitations (SD), based on a single restricted Hartree−Fock (RHF) reference.[35] Due to the single reference nature of this approach, the potentials are only reliable near the equilibrium geometry. Single reference based methods give incorrect molecular dissociation, as evidenced by the rapid increase of T_1 diagnostic value far away from the equilibrium geometry.[36] We include scalar relativistic effects for Cu through the second order Douglas-Kroll-Hess (DKH) Hamiltonian and apply a compatible correlation consistent basis set, aug-cc-pwCVTZ.[37−40] The closed-shell EOM-CCSD and the following CCSD(T) calculations were carried out with the MOLPRO code.[41] For excited states, the effect of spin−orbit coupling was also considered as this may mix the electronic singlet and triplet states. Our main interest was in the characterization of the A state, to which the transition from the ground state is spin forbidden. Spin−orbit coupling mixes the $A(^3\Pi_u)$ and $B(^1\Sigma_u^+)$ states as follows:[42]

$$\begin{pmatrix} E(^3\Pi_u) - \xi/2 & \sqrt{6}\xi/2 \\ \sqrt{6}\xi/2 & E(^1\Sigma_u^+) \end{pmatrix} \qquad (1)$$

where ξ is the spin−orbit coupling of Cu atom (0.1 eV). The relative energies of the A and B states were calculated by using the DKH-EOM-CCSD/aug-cc-pwCVTZ method, based on unrestricted Hartree−Fock (UHF) reference. This single point calculation was carried out with the Gaussian 09 code.[43]

The ground state Cu−He and Cu_2−He calculations employed the standard CCSD(T) method (core orbitals 1s, 2s, 2p, 3s, 3p on both Cu atoms), where in addition to single and double excitations, iterative triples were included.[44,45] Given the very weak van der Waals-type interaction, it was necessary to employ a large basis set, aug-cc-pV5Z (AV5Z),[40,46] to treat electron correlation to high accuracy, and to apply the basis set superposition error (BSSE) correction to remove deficiencies from using an incomplete basis set.[47] The calculation was carried out for He−Cu_2−He supermolecule within D_{2h} symmetry, with the resulting energies divided by two to give the effective Cu_2−He interaction. Note that the He−He interaction at the distances of relevance have negligible contribution to energy.

The applied bosonic density functional theory (DFT) model to describe superfluid helium and the numerical implementation has been described previously.[48−50] The ground state solutions for the liquid interacting with Cu or Cu_2 at 0 K temperature were obtained by the imaginary time propagation method with a 40 fs time step and a $256 \times 256 \times 256$ spatial grid with a grid step of 0.4 Bohr. The droplet energies were evaluated by numerically integrating the resulting energy density.

■ RESULTS

Copper Atoms. Time-gated fluorescence images of the ablation plume are shown in Figure 2a. Each image is obtained as 40 averages, with a gate width of 100 ns, at the indicated gate delay relative to the ablation laser pulse. The expansion is against cold helium vapor
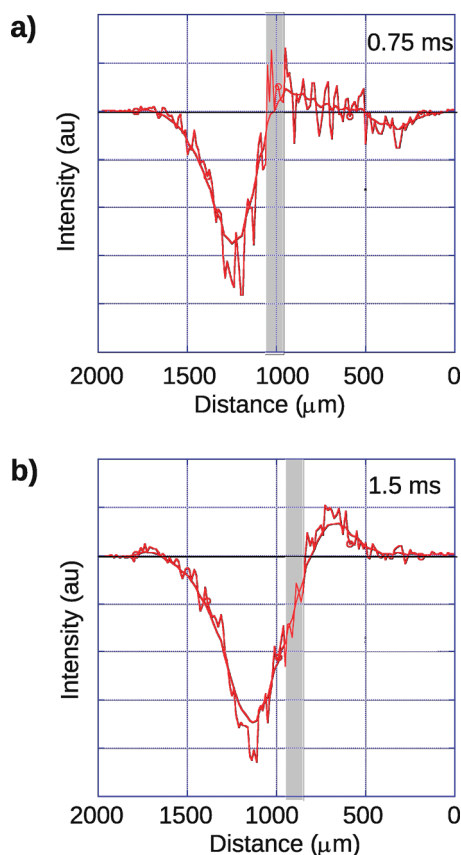
Figure 3. The differential spatial distribution of Cu atom fluorescence obtained as $I_{on}-I_{off}$ (averaged along the axis parallel to the copper target surface). The gray vertical band represents the location of the fountain. The dip in the distribution is the shadow cast by the opacity of the fountain (sum of inelastic and elastic scattering), while the positive peak in front of the fountain represents reflection at normal incidence. The indicated times are the time delays between the excimer and dye lasers, as in Figure 2b. At 1.5 ms, the Cu atom translation is thermalized, the motion is diffusive.
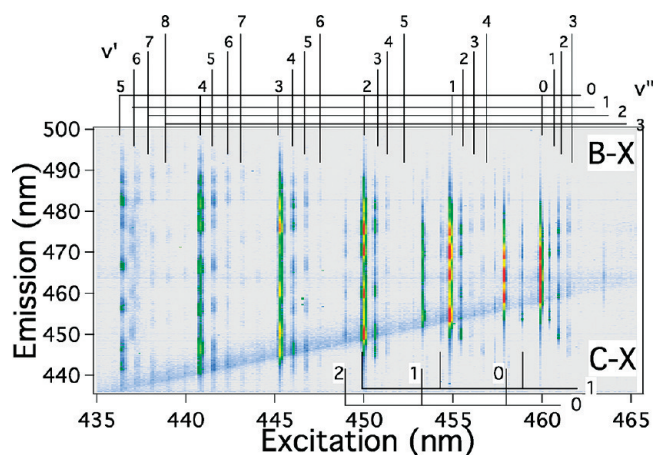

Figure 4. Two-dimensional excitation−emission spectrum of Cu_2 in dense helium gas at $T = 20$ K (contour colors represent the fluorescence intensity in arbitrary units with red and blue corresponding to high and low intensity, respectively). Both B ← X and C ← X vibronic transitions are labeled in the graph.

($P = 10$ Torr, $T = 1.7$ K). The front of the mushroom-shaped plume at 150 ns is at 400 μm from the ablation target; it evolves into a crescent at $t \sim 200$ ns, characteristic of detached shock front with a bow velocity of 10^3 m/s; post $t \sim 300$ ns, the directed motion is arrested and the plume evolves into isotropic expansion. To follow the history of the expansion post 500 ns (limited by the radiative lifetime of the metastable Cu $3^2P_{3/2}^0 \rightarrow 3^2D_{5/2}$ emission; $\tau_{rad} = 500$ ns),[51] we resort to laser induced fluorescence (LIF) imaging. We use a doubled dye laser tuned to the atomic $4^2S_{1/2} \rightarrow 3^2P_{3/2}^0$ transition at 324.75 nm, while monitoring the $3^2P_{3/2}^0 \rightarrow 3^2D_{5/2}$ transition at 510.55 nm.[51] LIF images of the Cu atom recorded at time delays as long as 1.5 ms are shown in Figure 2b. In this duration, the principal change in the distribution is the reduction of the atom number density in the probed volume. This can be discerned from the reduction in the vertical width of the fluorescence, which is due to fluorescence reabsorption and radiation trapping in the dense Cu gas. The effect allows the estimation of the atom number density as 10^{13} cm^{-3} as the cloud reaches the fountain location at $t = 150 \mu$s.[52] Note, the atom distribution appears to stagnate between target and fountain during the ~ 1 ms time of observation. This would be expected for a thermal velocity distribution undergoing diffusive expansion. At $T = 2$ K, a diffusion constant of $D = 2 \times 10^{-6}$ m^2/s is

to be expected, therefore an isotropic expansion of $(Dt)^{1/2} \sim 50 \mu$m in 1 ms, somewhat larger than the observed spreading of $\sim 30 \mu$m/ms. In effect, the atomic translational distribution is thermalized on the time scale of 1 ms.

The positions of the target surface and the fountain are marked in Figure 2b, at $t = 750 \mu$s the atom cloud extends past the fountain. The effect of the fountain on the spatial distribution of atoms, along the path of the dye laser, is obtained by recording LIF images with fountain on and off. Difference plots of the spatial LIF distribution, $I_{on}-I_{off}$, recorded at $t = 750 \mu$s and 1.5 ms, are shown in Figure 3. Upon turning the fountain on, a total deficit in LIF intensity of 20−40% develops behind it. The depletion reaches its maximum depth ~ 2 diameters behind the fountain: a shadow cast by an opaque fountain. Preceding the loss curve, there is a clear pile-up of LIF in front of the fountain, in the 1.5 ms data (Figure 3b). The effect is much smaller, in the 750 μs data (Figure 3a). In these direct line-of-sight measurements (where the dye laser crosses the fountain at 90°, see geometry in Figure 1a), pile-up of atoms at the front of the fountain implies reflection at the gas−liquid interface. Note that the lost atom flux, which significantly exceeds the reflection pile-up, does not have a unique interpretation. Deflection of the flux out of the plane of observation (defined by the intersection of the fountain and the dye laser beam) would explain the shadow cast behind the fountain. Alternatively, entrapment in the bulk or surface of the fountain would lead to the same depletion pattern given that the fluorescence of wet atoms is quenched. We have searched but failed to find spectroscopic signatures of entrained atoms. Independent of this, the clear identification of reflection at normal incidence necessarily implies that deflection must con-tribute to the observed depletion of LIF. The robust conclusion is the observation of efficient reflection of Cu atoms when their translation is thermalized to ~ 1.7 K in 1.5 ms (see Figure 3b). We should point out that the observed reflection pile-up at the front of the fountain also establishes that aspiration (Venturi effect) does not play a significant role in determining the gas density profile at the liquid−gas interface.

Copper Dimers and Cu_2−He_n Complexes. Copper dimers are formed efficiently in the Knudsen layer, where the ablation plume and the helium gas interpenetrate.[53] This is established

Table 1. Parameters for X, A, a, a′, B, and C states of Cu₂ molecule.^{a}

state	T_e^b	T_e^c	T_e^d	R_e^b	R_e^c	R_e^d	ω_e^b	ω_e^c	ω_e^d	$\omega_e x_e^b$	$\omega_e x_e^c$	lifetime
X ($^1\Sigma_g^+$)	0	0	0	2.22	2.22	2.25	275	266.5	251	1.4	1.04	
a ($^3\Sigma_u$)		15420	16450		2.48			125				
a′ ($^3\Sigma_g$)			18710									
A ($^3\Pi_u/^1\Sigma_u^+$)^e		20431	20000		2.28			192.5			0.35	
B ($^1\Sigma_u$)	21767	21758	22260	2.32	2.33	2.38	244 ± 1	246.3	216	2.1 ± 0.1	2.2	20^c, 200^d
C ($^1\Pi_u$)	21875	21866	22660	2.29	2.26	2.25	218	221.4	240	0.5	1.76	1000^c, 1000^d

^{a} The electronic origin T_e is given in cm^{-1}, harmonic and anharmonic frequencies ω_e and $\omega_e x_e$ are in cm^{-1}, equilibrium bond length R_e in Å, and radiative lifetime in ns. ^{b} Experimental data obtained in this work. The bond lengths were obtained through the analysis of Franck–Condon factors assuming that the ground state bond length is 2.22 Å. ^{c} Data from previous work.[29−33,54] ^{d} Theoretical calculations in this work. ^{e} Spin–orbit mixing with the B state makes the A state partially allowed.
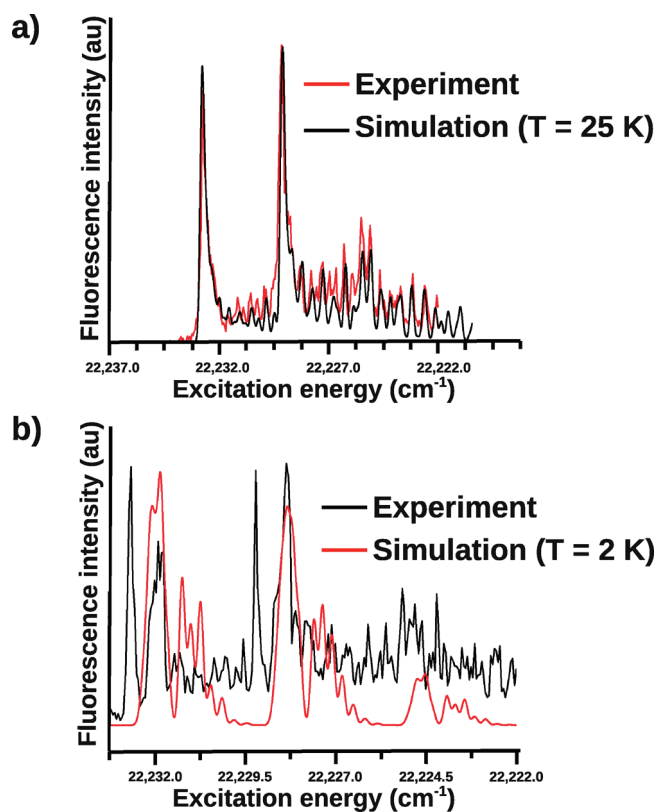
a)

b)

Figure 5. High-resolution spectrum of Cu₂ corresponding to B($v' = 2$) ← X($v'' = 0$) transition at 25 K (panel a) and 2 K (panel b).

spectroscopically, through two-dimensional excitation–emission spectra as shown, for example, in Figure 4. At the relatively elevated temperatures of $T \sim 2.9$–20 K, over a reservoir of normal helium, the observed spectra can be understood as those of bare Cu₂. There is not a clear signature of complexation with helium within the resolution of the spectral record. The spectrum is dominated by the B($v = 0, ..., 5$) ← X($v = 0$) progression, along with sequences built on X($v = 0, ..., 4$). In addition, three weaker vibrational transitions to a state nested in B can be identified. Access to these states leads to emission from the nearest lying vibrational level of the B state. This is directly established in the 2-D spectra by comparing the emission from each accessed state (vertical axis in Figure 4). The lines can be assigned to C ← X, placing the C state 80 cm^{-1} above B. The extracted spectroscopic constants are collected in Table 1. The B state vibrational constants, Franck–Condon (FC) factors, and

electronic origins are nearly identical to those of the bare molecule. Based on the FC factors, we find $|R_X − R_C| = 0.07$ Å, to be compared with the literature value of 0.04 Å; and $|R_X − R_B| = 0.10$ Å, to be compared with the literature values of 0.11 Å.[29−33,54] The equilibrium bond length in the C state is closer to the X state than in the B state, but overall, the bond lengths are very similar in all three states.

In Figure 5a we show a high-resolution segment of the B($v = 2$) ← X($v = 0$) line, recorded using an intracavity etalon. The spectrum at 20 K is perfectly reproduced with the known molecular constants, including the unusual isotope dependent electronic origins.[33] The fit determines the rotational temperature of the dimer to be the same as the gas temperature. We generally find that at time delays $t > 0.1$ ms, the rotation of the dimer is fully thermalized and the vibrational populations are frozen out. In contrast with the 20 K spectrum, the high-resolution excitation spectrum at 2 K (Figure 5b) cannot be reproduced under the assumption of bare Cu₂. While the rotational envelope of the molecule shows thermalization at $T_{rot} \sim 2$ K, there is significant mismatch between observed and predicted lines. There now are additional sharp lines in the observed spectrum, suggestive of transitions belonging to Cu₂–He. Given the sharp resonance, the transition must terminate on a bound long-lived excited state of the complex. Based on the calculated interaction potentials on ground and excited states, we will assign this species to a T-shaped Cu₂–He complex.

Ablation over pumped superfluid helium at temperatures below 2 K generates a new progression, as seen in the excitation–emission spectrum of Figure 6a. The excitation progression is blue-shifted from that of B ← X by 580 cm^{-1}. The emission origin of the new progression appears on a diagonal shifted from that of the excitation origins, indicating that each state emits after losing the same amount of energy. The emitting states are easily assigned to bare Cu₂(B → X) based on their FC patterns, as shown in Figure 6b. Since the spectrum only develops at $T < 2$ K, it must be assigned to a weakly bound complex in the ground state. The displaced origin line clearly shows that the complex undergoes vibrational predissociation in the B state, to emit as bare Cu₂. Closer inspection of the trace shown in Figure 6a reveals modulated excitation profiles, which are much broader than those of the bare molecule. They show unresolved blue tails with an envelope that is characteristically modulated at ~ 30 cm^{-1}, structure that must be associated with vibrations of the complex in the excited state. The excitation profiles also show modulation of ~ 12 cm^{-1} on the red edges, structure that must arise from the populated vibrational states of the complex in the ground state. Based on either the widths of the
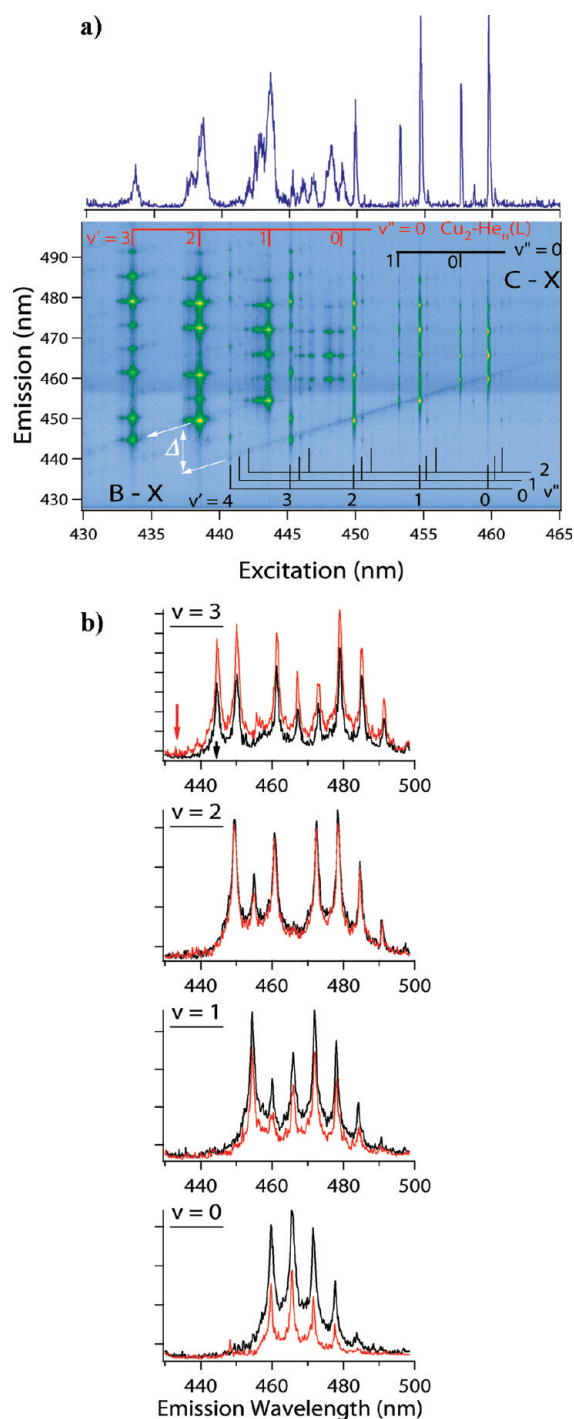
Figure 6. (a) Two-dimensional excitation—emission spectrum of Cu_2 in pumped helium at $T = 1.7$ K (contour colors represent the fluorescence intensity in arbitrary units with green and blue corresponding to high and low intensity, respectively). The trace shown is obtained by integrating over the emission coordinate (vertical axis). The diagonal where excitation and emission wavelengths coincide represents the line of origins (unrelaxed emission) of the dimer. The shifted diagonal represents fluorescence after vibrational predissociation of the Cu_2—He complex, where Δ is the energy difference between the excited state and the emitting state. (b) Except for the shift in excitation origin (indicated with arrows for the $v = 3$ transition), the fluorescence spectrum from the complex (red) and the dimer (black) are identical. The structure in the emission spectrum is dictated by Franck—Condon factors of the Cu_2 ($B \rightarrow X$) transition.

excitation profile, or on the relative intensity of the relaxed emission to that at the origin, a vibrational predissociation time of $1-3$ ps can be estimated. We infer that Cu_2 complexed to helium in a well-defined structure is being seen. In contrast to the sharp lines observed in the complex identified in the high-resolution spectrum (Figure 5b), the key to the structural assignment of this complex rests on the well-defined predissociation energy of about 600 cm^{-1}. This represents the excited state repulsive energy along the $Cu_2(B)$—He_n coordinate at the ground state equilibrium geometry of $Cu_2(X)$—He, which is predicted to occur for linear Cu—Cu—He interactions based on the calculations to be presented below. However, the calculations predict a repulsive energy of only 100 cm^{-1} for the linear complex. As such, we refer to this species as Cu_2—$He_n(L)$ to identify that it must contain linear interactions, and that the complex may contain more than one helium atom.

Cu_2—He Dry Cluster Nucleation and Growth. The above already establishes that transport of Cu dimers through cold helium vapor leads to complexation with helium. We see variations in the spectra with the conditions of ablation, pressure and temperature of the vapor, and time and distance at which the dimers are intercepted with the excitation laser. A useful method to understand the transport and formation dynamics of various species is through excitation imaging: recording the spatial distribution of fluorescence as a function of excitation wavelength at a given delay between ablation and re-excitation. Examples of excitation imaging are shown in Figure 7, along with an image of the fountain and the spatial distribution of the fluorescence. The background signal without the ablation laser is shown in Figure 7a where the tip of the fountain is visible at the bottom. The image in Figure 7b was recorded 1.5 mm above the fountain, with the fountain idling in the blob-mode, whereas a free-standing liquid fountain extends over the full height in Figure 7c. Cuts along the spatial coordinate, Figure 8a, show the evolution of the spectrum as a function of distance traveled. After traveling a distance of $d = 1$ mm from the ablation target, only the sharp progression of $Cu_2(X, v = 0)$ is seen. As the molecules approach the fountain, at $d = 2$ mm, the progression starts developing blue wings (see Figure 8a). The wings grow continuously over the fountain, and well past it. We see the continuous growth of a helium cluster as the molecules travel through the cold vapor. The nucleation occurs as the molecules enter a wide cone subtended by the blob; and once initiated, the growth is continuous. The cone can be associated with a region of denser (colder) helium in this pumped geometry. Nevertheless, the growth is a homogeneous, gas phase, without direct contact with the liquid. As such, we refer to these clusters as dry Cu_2—He_n. Their spectral signature is a vibrational progression that builds on the Cu_2 (B, C ← X) progressions, with a sharp red edge and a long blue tail that grows in intensity as a function of distance traveled (Figure 8a).

Cu_2—He Wet Cluster Growth. The excitation image in Figure 7c was obtained with the fountain turned on. The spectral cuts as a function of distance from the fountain are shown in Figure 8b. An evolution similar to the case of the dry clusters is seen, with the principal difference in the spectral signature being the disappearance of the sharp red-edge of progressions. The difference is suggestive of not only a size difference between dry and wet clusters, but also of embedding of the molecule. A sharp edge would imply access of zero-phonon lines. Their disappearance implies a solvation structure in which the excited and ground states shift relative to each other along the solvation
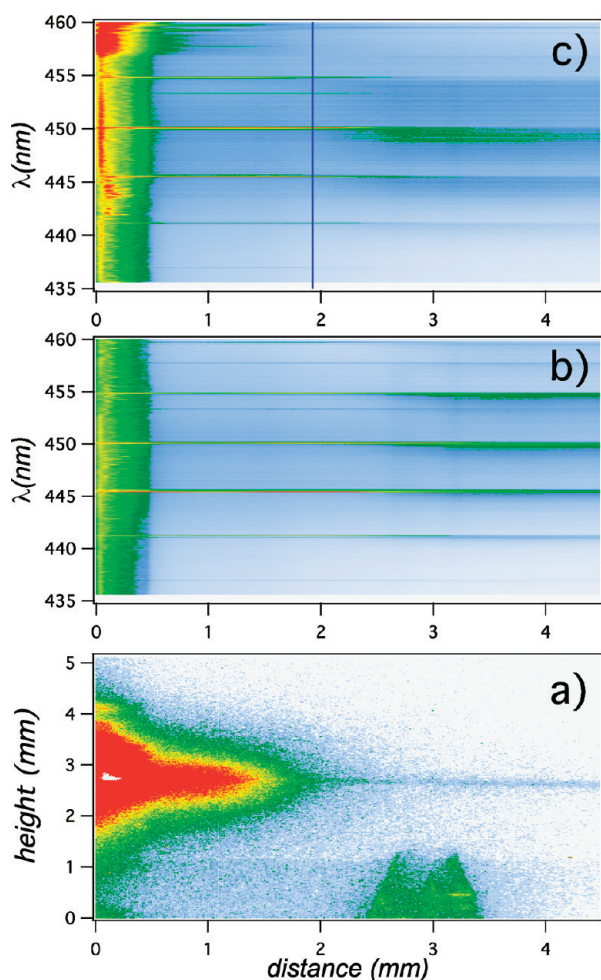
Figure 7. Fluorescence images of (a) spatial background signal without laser ablation (the fountain spout is visible at the bottom via light scattering); (b) excitation image of Cu_2 when the fountain is in the blob mode below the ablation/interrogation line that can be seen in (a); (c) excitation image of Cu_2 when the fountain crosses the ablation/interrogation line. In (b) and (c), the y-axis corresponds to the excitation wavelength. Note that in the latter two panels the LIF signal was averaged over the spatial y-direction (along the copper target) to enable 2D contour presentation. The x-axis in all panels corresponds to the distance from the ablation target. The contour colors represent the emission intensity in arbitrary units with red and blue corresponding to high and low intensity, respectively.

Figure 8. (a) Spectral cuts from Figure 7b at the indicated distances from the ablation target. (b) Spectral cuts taken from Figure 7c.

coordinate. This characteristic difference suggests that in the dry clusters the molecule remains near, or on, the surface, while in wet clusters, the molecules are embedded. The evolution of these spectra illustrates sensitivity to size, and structure. The more remarkable observation in the excitation images is the absence of any signature of the fountain. Any interaction, reflection, entrainment, condensation by formation of large copper clusters, would be expected to leave a vertical trace in the image at the fountain position, either due to enhanced or reduced fluorescence from the dimers, or any other new species.

Cu_2−He(liq) Injection and Transmission through the Fountain. To ensure that we observe the spectrum of the dimer in the liquid phase, without being overwhelmed by the signal from the surrounding clusters, we operate the fountain in its misty mode − where a fine mist is sprayed by the boiling
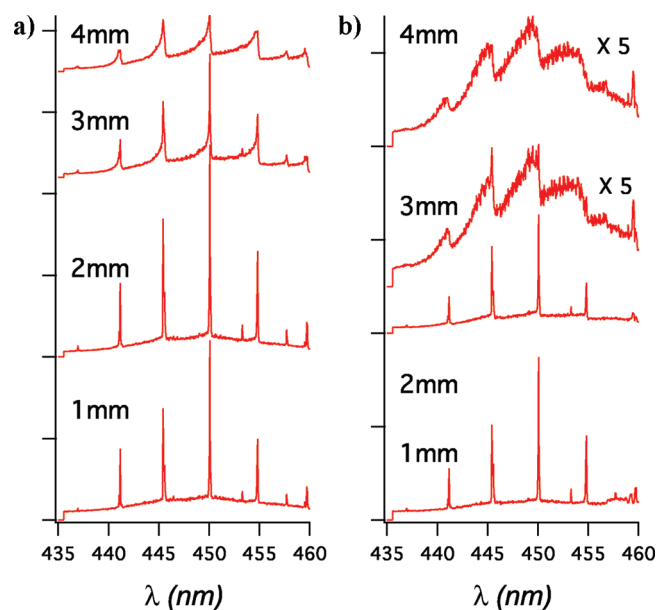
fountainhead (Figure 1). The excitation image is shown in Figure 9a, a cut along the spatial coordinate is shown in Figure 9b, and two spectral cuts, before and after the fountain, are shown in Figure 9c. The very broad spectrum, in which the dimer progression is only apparent as a weak modulation, can be safely assigned to Cu_2−He(liq). Note the sharp lines that appear in the spectrum behind the fountain belong to the blue-shifted progression of Cu_2−He_n(L). Again, the liquid spectrum can be discerned in the baseline of the spectrum before the fountain, signifying molecules in droplets. In this case, the dimer spectra effectively terminate at the fountain, and the fountain can be directly visualized in the excitation image (Figure 9a). This is reenforced in the density profile of fluorescers, taken as a spatial cut across the fountain (Figure 9b). The fluorescence peak at the fountain clearly demonstrates build-up in the local density of Cu_2, and therefore entrainment. No such feature could be seen in the nondivergent flow of Figure 7c. The spike in Figure 9b is over a smoothly decaying density profile, suggesting that a significant fraction is transmitted through the fountain. Subtraction of the background distribution with fountain off, shows a small deficit of liquid dimers around the fountain. There is no evidence of reflection of the molecules carried by the droplets at the interface, as there was in the case of the atoms.

Entrainment in the Columnar Fountain. Copper dimers can be completely entrained in the faster column flow. We illustrate this through spatial images recorded at selective wavelengths, designed to enhance contrast between the liquid spectra and bare dimers. In Figure 10a we show a fluorescence image recorded with 438 nm excitation, in which the emission from entrained molecules from the fountain can be seen in the shape of the column. The excitation is shifted from the diatomic resonances, and the ablation intensity is adjusted to optimize loading of the fountain. Cuts at several delays and wavelengths are shown in Figure 10b and c, respectively. These are obtained after subtracting the background signal obtained in the absence of the fountain. The dimer distribution between target and fountain can be seen in addition to the entrained molecules. In sharp contrast with the misty fountain, now the backside of the fountain is
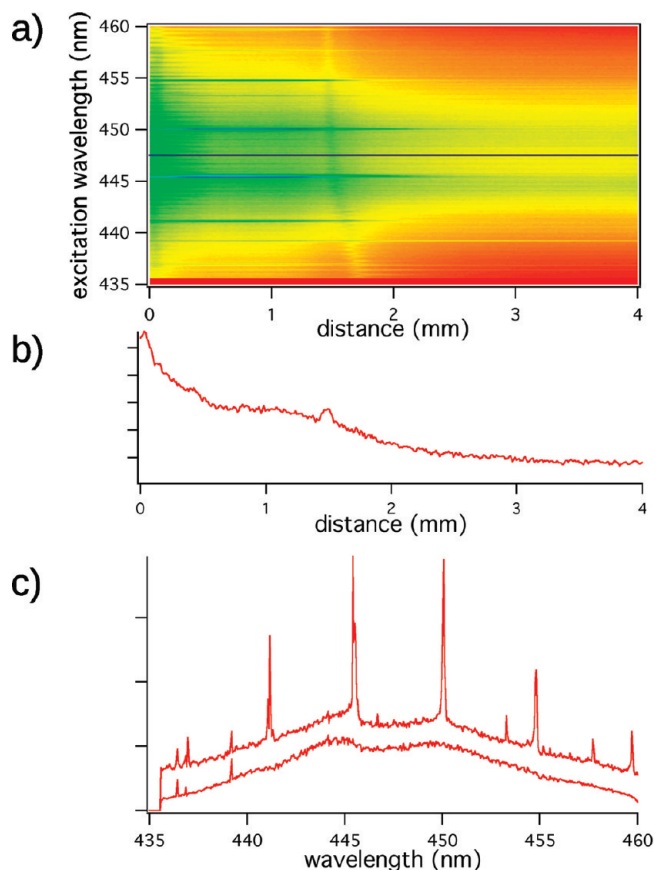
Figure 9. Fountain in misty mode operation. (a) Two-dimensional excitation−emission spectrum (x-axis corresponds to the distance from the ablation target; y-axis is the excitation wavelength; contour colors denote the fluorescence intensity in arbitrary units with green and red representing high and low intensity, respectively), (b) horizontal cut along the line shown in (a) represents the distance-dependent distribution of the fluorescing dimers. The peak at the fountain, at 1.5 mm from target, indicates entrainment. (c) Spectral cuts before and after the fountain (at 1 mm and 3 mm, respectively) show the complete blending of the diatomic lines into the broad (liquid) spectrum. The surviving sharp lines between 435 and 440 nm are from linear complexes.

dark; trapped molecules cannot exit the sharp interface. The cross-sectional set recorded as a function of excitation delay, gives a qualitative picture of the velocity dependent trapping probabilities. In the case shown, the maximal loading occurs at a delay of 2 ms.

■ DISCUSSION

Copper Dimer. Although there has been extensive spectroscopy on Cu_2, the existing theoretical analysis of the excited states is limited.[55,56] It is therefore useful to consider the spectroscopically relevant molecular potentials in a consistent calculation. The calculated low-lying excited electronic singlet Σ, Π, and Δ states of Cu_2 are shown in Figure 11. It was necessary to include the DKH Hamiltonian in the calculation with the appropriate DKH compatible basis set to obtain correct energetics for the states. In addition to serious convergence issues, the attempted multireference configuration interaction calculations were extremely sensitive to the active space chosen and the associated rapid increase in the computational demand. The EOM-CCSD method, on the other hand, was more robust in converging to the correct states around the equilibrium
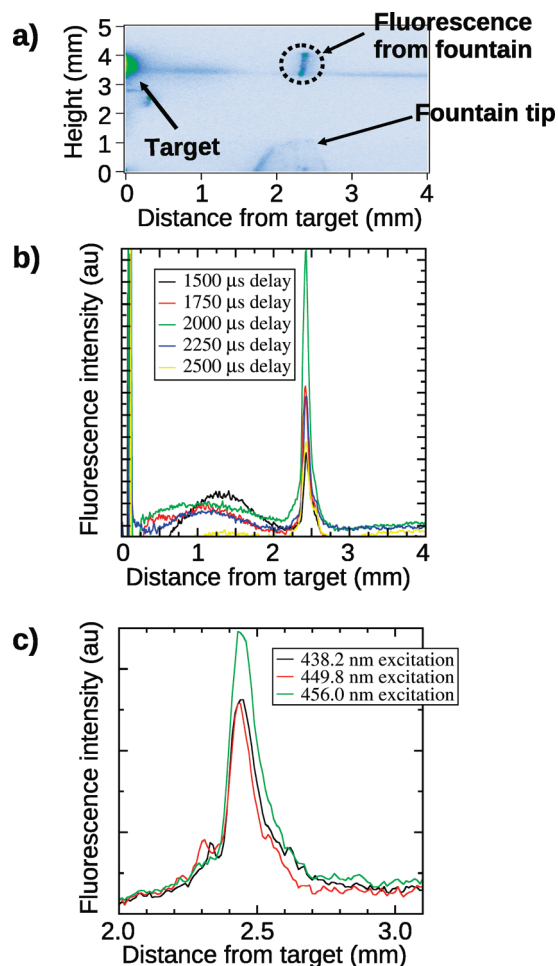

Figure 10. (a) Spatial fluorescence image demonstrating the loading of the columnar fountain (excitation at 438.2 nm; contour colors represent the emission intensity in arbitrary units with green and light blue corresponding to high and low intensity, respectively); (b) Time evolution of the fountain loading (maximum loading at 2000 μs), given by the delay time between ablation with the excimer pulse and interrogation with the dye laser pulse; (c) Cu_2 fluorescence image inside the fountain at selected excitation wavelengths.

distance but due to the single reference nature of the method, it failed after about 3 Å distance as the T_1 norm increased rapidly exceeding the suggested value in the literature (0.02).[36] The radiative lifetimes of the B−X and C−X transitions were evaluated from the transition dipole moments between states and Einstein coefficient of spontaneous emission. For the A state only, a single point calculation was carried out since the computational expense of UHF based EOM-CCSD is fairly high and the current experiments focused on the X, B, and C states. The effect of the spin−orbit coupling to mix the A and B states has a negligible effect on the energetics of the states (eq 1) but allows the A state to borrow intensity from the B state through the mixing. This makes the A−X transition weakly electric dipole allowed. The relevant potential parameters for the X, A, B, and C states are summarized in Table 1, and a comparison between the calculated and available experimental data is provided. The crossing point between the B and C states lies almost directly above the X ground state, giving a high degree of overlap between B and C state vibronic wave functions. In the present measurements, the C state rapidly converts to B and the fluorescence is observed mainly from the

B state. The calculated equilibrium bond lengths, electronic origins and radiative lifetimes are in fair agreement with the experimental data, the harmonic vibrational frequencies are only of the correct magnitude but the relative orders between the B and C states are reversed. The most likely factor limiting the accuracy of the current
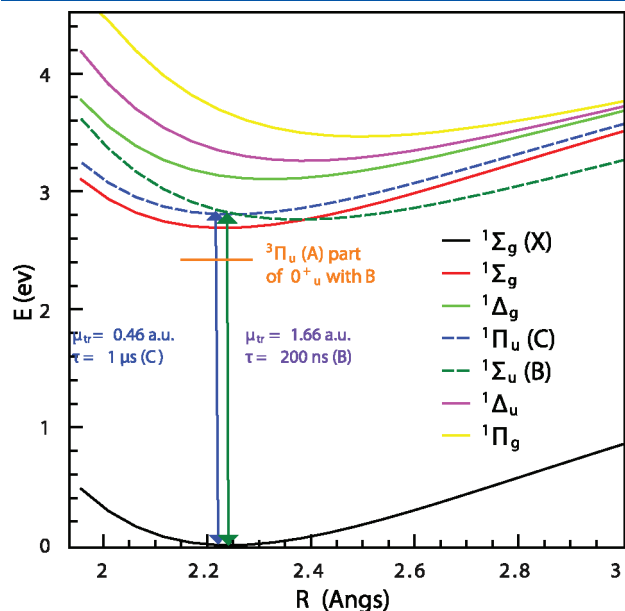

Figure 11. Ground and several excited states of Cu_2 from RHF-EOM-CCSD calculations. The A state was obtained from a single point calculation employing the UHF-EOM-CCSD method.
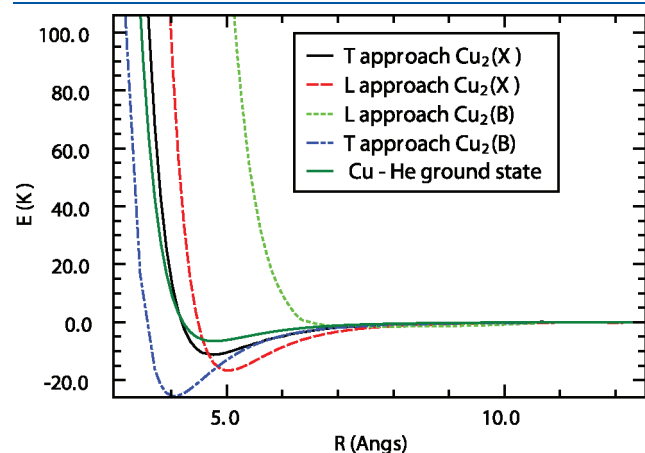

Figure 12. Calculated interaction potentials between Cu—He (CCSD(T)), $Cu_2(X)$—He (CCSD(T)), and $Cu_2(B)$—He (EOM-CCSD).

calculations is the applied triple-ζ level basis set. At the present level of accuracy, the calculations fully support the experimental assignment of states and observations at the reported resolution, of otherwise well-known spectroscopy.[29-33]

Copper Atom Scattering at the Liquid Interface. The theoretically extracted Cu—He potential is shown in Figure 12 and its parametrization is given in Table 2. The interaction is weak, characterized by a potential well depth of 4.8 cm^{-1}, slightly more than half the depth of the He—He potential.[57] Energetics in such shallow potentials will be sensitive to the long-range part of the interaction, which in the present is of limited reliability. As such, the fitted form should be used with caution. The parametrized potential supports one bound rotationless state and one bound state in the $J = 1$ centrifugal potential (see Table 3). Cu can be regarded as "heliophobic" and, as such, is expected to prefer surface attachment rather than penetrate to the bulk.[58] This, we verify explicitly, through bosonic DFT calculations of the energetics of Cu on a droplet with 1000 helium atoms. Due to the summation of the van der Waals interaction, the binding energy of Cu on the surface of the droplet is 22 K. Nevertheless, the atom is unstable when embedded in the droplet; the free energy of the system is minimized with the atom bound to the surface. This can be understood as the effect of minimizing the cavity energy in a finite size droplet.

The most important observation regarding Cu atoms in the present is their scattering dynamics at the fountain interface. We observe the scattering dynamics in ~2 K isotropic collisions at the surface to be dominated by reflection. Given a surface binding energy that is an order of magnitude larger than the kinetic energy of collision, in classical gas—liquid scattering, efficient trapping and negligible reflection would be expected.[59] In classical scattering, multiple collisions at the dynamically disordered surface would ensure energy loss, especially where the collision energy is the same as the temperature of the liquid. Although to date limited to helium atoms, a very different picture controls quantum scattering at the gas-superfluid interface. The classic reflection measurements of helium atoms from the free surface of superfluid helium[60,61] confirmed the earlier suggestions by Anderson[62] and Widom[63,64] that quantum evaporation or scattering is controlled by a single particle event, the creation or annihilation of a single phonon or roton. This occurs on the attractive part of the interaction potential, in contrast to classical scattering, which is dominated by hard-core collisions. At any angle of incidence a Cu atom can create a 2 K phonon to fall into the bound part of the Cu—He(Liq) potential. However, this does not constitute condensation. From such a precursor state, either additional excitations have to be generated to trap or the atom can re-evaporate with the annihilation of a thermally populated phonon (or roton). With detailed balance in mind, it is clearer to consider the evaporation of a bound Cu atom.

Table 2. Parametrized Potentials Fitted to the Form: $V(r) = a_0 \exp(-a_1 r) - a_2 r^{-6} - a_3 r^{-8}$, in Å $-cm^{-1}$ Units (for Fitting Purposes Only)^a

	Cu—He	L—$Cu_2(X)$—He	T—$Cu_2(X)$—He	L—$Cu_2(B)$—He	T—$Cu_2(B)$—He
a_0	1.1×10^6	5.0×10^6	2.1×10^6	3.6×10^6	2.2×10^6
a_1	2.544	2.446	2.590	1.973	2.814
a_2	7.661×10^4	7315	1.236×10^5	39.81	1.326×10^5
a_3	1.079×10^6	1.383×10^7	1.723×10^6	3.357×10^7	8.878×10^5
r_{min}	4.8	5.0	4.8	7.2	4.1
V_{min}	4.6	11.7	7.9	~ 2	17.8

^{a} r_{min} and V_{min} correspond to the minimum energy distance and energy, respectively. T and L denote the linear and T-shaped geometries.

Table 3. Rotation-Vibration States of $Cu_{(1,2)}-He$

v	J	cm^{-1}
Cu—He		
0	0	−0.86
	1	−0.016
L—Cu_2(X)—He		
0	0	−12.8
	1	−11.7
	2	−9.64
	3	−6.54
	4	−2.52
1	0	−2.11
	1	−1.47
	2	−0.26
2	0	$−1.2 \times 10^{-5}$
T—Cu_2(X)—He		
0	0	−7.77
	1	−6.63
	2	−4.39
	3	−1.16
1	0	−0.53
	1	−0.04
T—Cu_2(B)—He		
0	0	−8.22
	1	−6.64
	2	−3.64
1	0	−0.28

The excitation must now overcome the binding energy of the atom, $V = 22$ K, and supply the additional kinetic energy, T, to reach the initial scattering state. Since $T + V$ exceeds that of the maxon (14.5 K),[6] the dispersion curve of the heavy atom, $E = p^2/2m + V$, does not cross that of helium. Neither quantum evaporation nor quantum condensation is possible, leaving elastic scattering as the main channel for the Cu atom interaction with the helium fountain.

Copper Dimer—Helium Interaction and Complexes. The interaction of ground state Cu_2 molecule with helium was calculated at the CCSD(T)/AV5Z level to provide an optimal account for treating electron correlation, which is essential in modeling van der Waals interactions. The results are shown in Figure 12 for linear ("L") and broadside ("T") approaches of helium. The linear geometry is more bound (17 K) than the T structure (11 K). For a freely rotating Cu_2 molecule in helium, in $J = 0$ state, it is more relevant to consider the rotationally averaged potential, which has a well depth of 13 K. We compute the bound rotational vibrational states of the L- and T-structures, subject to the additional centrifugal potential:

$$V(r,J) = V(r) + \frac{J(J+1)}{2\mu r^2} \qquad (2)$$

The bound states and their energies are listed in Table 3. The results are subject to the same cautionary comments made in the Cu—He discussion; the long-range part of the potential can significantly alter the obtained binding energies. This will not change the findings that in the T-complex the binding of He to Cu_2 is stronger in the B state (see potentials in Figure 12) and

that the vibrational level spacings in X and B states are quite similar (see Table 3). At $T = 2$ K, several rotation-vibration states should be populated in the ground state and a sharp line spectrum is to be expected in these bound—bound transitions. The perturbed high-resolution line spectrum seen at $T = 2$ K in Figure 5 is only consistent with the T-structured complex. The spectrum contains one prominent sharp line accompanying each isotopic origin of bare Cu_2 (the line not reproduced by the simulation), with a blue shift of 0.16 cm^{-1}. Only one prominent line above the origin is expected for the complex, namely, the $v' = 0$, $J' = 1 \leftarrow v'' = 0$, $J'' = 0$ transition, for which a blue shift of 1.1 cm^{-1} is predicted (see Table 3). We take this qualitative agreement as the basis for assigning the spectrum to the T-shaped complex (T—Cu_2—He).

In the linear 1:1 complex, the excited B state potential does not sustain a bound state (Table 3). The vertical energy difference, $\Delta V(r_{min}) = V(B) - V(X)$, at the potential minimum of the ground state is 100 cm^{-1}. To rationalize the spectrum assigned to $Cu_2—He_n(L)$, which appears as a complete sequence shifted by ∼600 cm^{-1} (Figure 6a), at least six such repulsive interactions are needed. Note that for broadside attachment the vertical energy difference is negligible, the present potential would account for only ∼200 cm^{-1} blue shift for a shell of He atoms, derived mainly from the two axial atoms He—Cu_2—He. This brings into question the accuracy of the potentials on the repulsive wall; however, does not change the qualitative predictions. The blue-shifted progression assigned to $Cu_2—He_n(L)$ must be associated to linear complexes that fall apart in the excited state to release the linearly bound He atoms. It is useful to estimate the time scale of predissociation by considering the time it takes for the overlap of the ground and excited states wave functions to decay along the Cu_2—He coordinate. This is defined by the time correlation function:

$$c(t) = e^{-t/\tau_{pre}} = |\langle \varphi^X(t=0)|\varphi^B(t)\rangle|^2$$
$$= |\langle \varphi^X(t=0)|e^{-iH_B t/\hbar}\varphi^X(t=|0\rangle)|^2 \qquad (3)$$

in which the time propagation is on the excited state L—Cu_2-(B)—He potential. A predissociation time of $\tau_{pre} = 2.8$ ps is obtained using the present potentials. This time scale also defines the minimum convolution width of ∼12 cm^{-1} that will contribute to any line transitions in the complex. This explains the absence of sharp structure in $Cu_2—He_n(L)$ spectra inspected at high resolution. We rationalize the blue-shifted progression as arising from Cu_2 linearly attached to at least one helium atom, and based on the energetics, it is more likely to have both axial wells occupied. This would include the possibility for a complete shell of helium atoms enclathrating the dimer.

The spectra obtained as a function of Cu_2 transport through the dense gas show a very different behavior. The dry clusters show blue tails that evolve continuously as the cluster grows, but without a shift of vibrational origins (see sharp edges in Figure 8a). Since a linearly bound He atom will lead to >100 cm^{-1} blue shift, it becomes apparent that the dry clusters correspond to structures in which the copper dimer lies flat on the surface of a growing He cluster. Above, we made this conclusion regarding Cu atoms. The broadening of the vibrational origins (Figure 8b) is then consistent with the dimer being solvated in the cluster, "wetting", whereby it is subject to both linear and T-interactions, as in our discussion of a full solvation shell shifting the electronic origin by 600 cm^{-1}. The binding

energy of the dimer to He is larger than for the atom and since it exceeds the cohesive energy of helium, we would expect dimers to embed in the larger clusters. This is supported by the bosonic DFT calculations, which predict that Cu_2 should reside inside helium droplets (the free energy of solvation nearly 150 K for a droplet with 500 He atoms). The experiment may be selective in identifying the surface bound molecules, which would be the case if, for example, nonradiative decay dominates the excited state relaxation in the bulk. Clearly, the excitation spectra of the dimer are strongly perturbed by attachment, or solvation in liquid helium. This is in stark contrast with the published LIF spectra of Cu_2, obtained by laser ablation in the bulk liquid and solid as a function of pressure where unperturbed molecular vibronic transitions are observed in emission.[16,19] Presumably, the emission there occurs in large enough bubbles to be completely impervious to the local helium environment. Given the large free energy of solvation of Cu_2 in helium, the observation that in general the transport of the cold molecules through the fountain is unimpeded (Figures 7 and 9) is nontrivial, even though, formally, there is no mechanism for scattering of particles that travel at speeds below the critical velocity of helium.

■ CONCLUSIONS

We described the realization of molecular injection in a superfluid helium fountain. The results are intriguing and promise a variety of applications with this uniquely flexible source and method. The utility for spectroscopic applications was highlighted through the analysis of the dimer spectra. A more rigorous treatment of the spectra will require numerical modeling. The platform also provides direct investigations of scattering processes, along which we gave two outstanding examples: quantum reflection of the atom, and unimpeded transmission of dimers through the fountain. These results are experimental observations that will require further scrutiny to be fully appreciated. Finally, we clearly show entrainment of molecules in a directed, nondivergent flow as a beam. Beyond the fundamental questions, entraining molecules in a homogeneous cold column opens up diverse applications. Focusing of the molecular column, for lithography or for homogeneous condensation,[65] bending and manipulating the beam by irradiation with an inhomogeneous intensity field of a laser are examples.

■ AUTHOR INFORMATION

Corresponding Author

*E-mail: aapkaria@uci.edu.

■ ACKNOWLEDGMENT

■ REFERENCES

(1) Toennies, J. P.; Vilesov, A. F. Rev. Phys. Chem. 1998, 49, 1.
(2) Toennies, J. P.; Vilesov, A. F. Angew. Chem., Int. Ed. 2004, 43, 2622.
(3) Toennies, J. P. Phys. J. 2002, 1, 49.
(4) Goyal, S.; Schutt, D. L.; Scoles, G. Phys. Rev. Lett. 1992, 69, 933.
(5) Khalatnikov, I. M. The Physics of Liquid and Solid Helium; Wiley: New York, 1976.
(6) Wilks, J. the Properties of Liquid and Solid Helium; Clarendon Press: Oxford, 1967.
(7) Hartmann, M.; Miller, R. E.; Toennies, J. P.; Vilesov, A. F. Phys. Rev. Lett. 1995, 75, 1566.
(8) Ghazarian, V.; Apkarian, J. E. V. A. Rev. Sci. Instrum. 2002, 73, 3606.
(9) Slipchenko, M. N.; Kuma, S.; Momose, T.; Vilesov, A. F. Rev. Sci. Instrum. 2004, 73, 3600.
(10) Claas, P.; Mende, S.-O.; Stienkemeier, F. Rev. Sci. Instrum. 2003, 74, 4071.
(11) Pentlehner, D.; Riechers, R.; Dick, B.; Slenczka, A.; Even, U.; Lavie, N.; Brown, R.; Luria, K. Rev. Sci. Instrum. 2009, 80, 043302.
(12) Bierau, F.; Kupser, P.; Meijer, G.; von Helden, G. Phys. Rev. Lett. 2010, 105, 133402.
(13) Jortner, J.; Meyer, L.; Rice, S.; Wilson, E. G. Phys. Rev. Lett. 1964, 12, 415.
(14) Dennis, W. S.; E.; Durbin, J.; Fitzsimmons, W. A.; Heybey, O.; Walters, G. K. Phys. Rev. Lett. 1969, 23, 1083.
(15) Kinoshita, T.; Fukuda, K.; Yabuzaki, T. Phys. Rev. B 1996, 54, 6600.
(16) Persson, J. L.; Hui, Q.; Nakamura, M.; Takami, M. Phys. Rev. A 1995, 52, 2011.
(17) Hui, Q.; Takami, M. J. Low Temp. Phys. 2000, 119, 393.
(18) Tabbert, B.; Beau, M.; Gunther, H.; Haussler, W.; Honninger, C.; Meyer, K.; Plagemann, B.; zu Putlitz, G. Z. Phys. B 1995, 97, 425.
(19) Lebedev, V.; Moroshkin, P.; Toennies, J. P.; Weis, A. J. Chem. Phys. 2010, 133, 154508.
(20) Allen, J. F.; Jones, H. Nature 1938, 141, 243.
(21) Brown, M.; Wyatt, A. F. G. J. Phys: Condens. Matter 1990, 2, 5025.
(22) Williams, C. D. H. J. Low Temp. Phys. 1998, 113, 11.
(23) Dalfovo, F.; Guilleumas, M.; Lastri, A.; Pitaevski, L.; Stringari, S. J. Phys.: Condens. Matter 1997, 9, L369.
(24) Vertes, A.; Dreyfus, R. W.; Platt, D. E. IBM J. Res. Dev. 1994, 38, 3.
(25) Autin, M.; Briand, A.; Mauchien, P.; Mermet, J. M. Spectrochim. Acta 1993, 48B, 851.
(26) Dreyfus, R. W. J. Appl. Phys. 1991, 69, 3.
(27) Gole, J. L.; English, J. H.; Bondybey, V. E. J. Phys. Chem. 1982, 86, 2560.
(28) Bondybey, V. E.; Schwartz, G. P.; English, J. H. J. Chem. Phys. 1983, 78, 11.
(29) Page, R. H.; Gudeman, C. S. J. Chem. Phys. 1991, 94, 39.
(30) Lochet, J. J. Phys. B 1978, 11, L55.
(31) Rohl_ng, E. A.; Valentini, J. J. J. Chem. Phys. 1986, 84, 6560.
(32) Ram, R. S.; Jarman, C. N.; Bernath, P. F. J. Mol. Spectrosc. 1992, 156, 468.
(33) McCaffrey, J. G.; Bennet, R. R.; Morse, M. D.; Breckenridge, W. H. J. Chem. Phys. 1989, 91, 92.
(34) Eloranta, J. A Simplified C Programming Interface for Research Instruments, http://sourceforge.net/projects/libmeas/, 2010.
(35) Korona, T.; Werner, H.-J. J. Chem. Phys. 2003, 118, 3006.
(36) Lee, T. J.; Taylor, P. R. J. Quantum Chem. 1989, S23, 199.
(37) Reiher, M.; Wolf, A. J. Chem. Phys. 2004, 121, 2037.
(38) Reiher, M.; Wolf, A. J. Chem. Phys. 2004, 121, 10945.
(39) Wolf, A.; Reiher, M.; Hess, B. A. J. Chem. Phys. 2002, 117, 9215.
(40) Balabanov, N. B.; Peterson, K. A. J. Chem. Phys. 3005, 123, 064107.
(41) Werner, H.-J.; et al. MOLPRO, version 2010.1, a package of ab initio programs; 2010, see http://www.molpro.net.
(42) Ermler, W. C.; Lee, Y. S.; Pitzer, K. S. J. Chem. Phys. 1979, 70, 293.
(43) Frisch, M. J.; et al. Gaussian 09, Revision A.1.; Gaussian Inc.: Wallingford, CT, 2009.
(44) ZHampel, C.; Peterson, K.; Werner, H.-J. Chem. Phys. Lett. 1992, 190, 1.
(45) Deegan, M. J. O.; Knowles, P. J. Chem. Phys. Lett. 1994, 227, 321.
(46) Woon, D. E.; T. H. Dunning, J. J. Chem. Phys. 1994, 100, 2975.

7087

dx.doi.org/10.1021/jp1123986 |J. Phys. Chem. A 2011, 115, 7077–7088

(47) Boys, F.; Bernardi, F. *Mol. Phys.* **1970**, *19*, 553.

(48) Dalfovo, F.; Lastri, A.; Pricaupenko, L.; Stringari, S.; Treiner, J. *Phys. Rev. B* **2005**, *72*, 214522.

(49) Lehtovaara, L.; Toivanen, J.; Eloranta, J. *J. Comput. Phys.* **2007**, *221*, 148.

(50) Lehtovaara, L.; Kiljunen, T.; Eloranta, J. *J. Comput. Phys.* **2004**, *194*, 78.

(51) Fuhr, J. R.; Wiese, W. L. *CRC Handbook of Chemistry and Physics*, 86th ed.; CRC Press: Boca Raton, FL, 2005.

(52) Ghazarian, V. Ph.D. Thesis; University of California, Irvine, 2005.

(53) Kelly, R.; Dreyfus, R. W. *Surf. Sci.* **1988**, *198*, 263.

(54) Morse, M. D. *Chem. Rev.* **1986**, *86*, 1049.

(55) Witko, M.; Beckmann, H.-O. *Mol. Phys.* **1982**, *47*, 945.

(56) Danovich, D.; Filatov, M. *J. Phys. Chem. A* **2008**, *112*, 12995.

(57) Janzen, A. R.; Aziz, R. A. *J. Chem. Phys.* **1997**, *107*, 914.

(58) Ancilotto, F.; Lerner, P. B.; Cole, M. W. *J. Low Temp. Phys.* **1995**, *101*, 1123.

(59) Nathanson, G. M. *Rev. Phys. Chem.* **2004**, *55*, 231.

(60) Edwards, D. O.; Fatouros, P.; Ihas, G. G.; Mrozinski, P.; Shen, S. Y.; Gasparini, F. M.; Tam, C. P. *Phys. Rev. Lett.* **1975**, *34*, 1153.

(61) Edwards, D. O.; Fatouros, P. P. *Phys. Rev. B* **1977**, *17*, 2147.

(62) Anderson, P. W. *Phys. Lett. A* **1969**, *29*, 563.

(63) Widom, A. *Phys. Lett. A* **1969**, *29*, 96.

(64) Hyman, D. S.; Scully, M. O.; Widom, A. *Phys. Rev.* **1969**, *186*, 231.

(65) Gordon, R. J.; Zhu, L.; Schroeder, A.; Seideman, T. J. *J. Appl. Phys.* **2003**, *94*, 669.